NANO LETTERS

2007
Vol. 7, No. 5
1138−1143

Metallic State in a Lime–Alumina Compound with Nanoporous Structure

Sung Wng Kim,[†] Satoru Matsuishi,[†] Takatoshi Nomura,[‡] Yoshiki Kubota,[§] Masaki Takata,[||,⊥] Katsuro Hayashi,[†] Toshio Kamiya,[‡] Masahiro Hirano,[†] and Hideo Hosono*[,†,‡]

Frontier Collaborative Research Center, Tokyo Institute of Technology, Mail Box S2-13, 4259 Nagatsuta, Midori-ku, Yokohama 226-8503, Japan, Materials and Structures Laboratory, Tokyo Institute of Technology, Mail Box R3-4, 4259 Nagatsuta, Midori-ku, Yokohama 226-8503, Japan, Department of Physical Science, Graduate School of Science, Osaka Prefecture University, 2-1 Daisencho, Sakai-ku, Sakai, Osaka 590-0035, Japan, Structural Materials Science Laboratory, Harima Institute, RIKEN SPring-8 Center, 1-1-1, Kouto, Mikazuki, Sayo, Hyogo 679-5198 Japan, and CREST, Japan Science and Technology Agency, Japan

Received November 21, 2006; Revised Manuscript Received December 25, 2006

ABSTRACT

We report a metallic state in a nanostructured porous crystal $12CaO{\cdot}7Al_2O_3$ by incorporating electrons in the inherent subnanometer-sized cages, in which a three-dimensionally closely packed cage structure acts as an electronic conduction path. High-density electron doping ($\sim 2 \times 10^{21}$ cm^{-3}), which was achieved by a thermal treatment in Ti metal vapor at ~1100 °C, induces homogenization of the cage geometry to a symmetric state, resulting in an insulator–metal transition with a sharp enhancement of the electron drift mobility from ~0.1 to 4 cm^2 V^{-1} s^{-1}. The results provide an approach for the realization of electroactive functions in materials composed only of environmentally benign elements by utilizing the appropriate nanostructures.

Nanostructured porous materials such as zeolites are attractive for versatile applications in chemistry and electronics. However, the expectation for electroactive functions has been limited to specific porous materials such as the carbon nanotubes because a highly conductive state is missing in other porous materials. Therefore, nanostructured porous materials constituted of a three-dimensionally periodic array of subnanometer-sized cages are attractive because this cage array would give rise to a metallic state if an electron is successfully doped to the cage to form a quantum dot.

The nanoporous crystal $12CaO{\cdot}7Al_2O_3$ (C12A7), which is a light metal oxide composed only of typical electronic insulators, lime, and alumina. Although this material is known as a constituent of alumina cement, no electroactive function had been reported. C12A7 has a cubic lattice (a = 1.199 nm) with a unit cell composed of a positively charged lattice framework, $[Ca_{24}Al_{28}O_{64}]^{4+}$. This framework has 12 subnanometer-sized cages and two extraframework O^{2-} ions ("*free oxygen ions*") in a unit cell (Figure 1).[4−6] The cages are three-dimensionally connected through a monomolecular-thick cage wall. Two out of the 12 cages are occupied by free oxygen ions, while the other ten cages are empty. The free oxygen ions may be replaced with electrons by reducing processes such as Ca vapor treatment. The complete replacement leads to the formation of $[Ca_{24}Al_{28}O_{64}]^{4+}(4e^-)$, which is regarded as a new type of inorganic electride. Theoretical analyses and experimental approaches have revealed that the cages in C12A7 form an additional conduction band called "*cage conduction band* (CCB)".[7−9] The CCB is located 1−2 eV below the bottom of "*framework conduction band*", which is primarily composed of Ca 5s orbitals. At low electron concentrations, the electrons induce a large lattice deformation due to the Coulomb attractive force between the entrapped electron and the two Ca^{2+} ions on the cage wall, causing electron localization. Consequently, the conduction occurs via the hopping of the electron from a localized deformed cage (an isolated quantum dot state) to the CCB (i.e., by *polaron*). This is the reason why the drift mobility is much smaller than 1 cm^2 V^{-1} s^{-1}, and the conductivity shows a thermally activated behavior in the electron-doped C12A7 reported previously.[1−3,10,11] Here we

* Corresponding author. E-mail : hosono@msl.titech.ac.jp. Telephone: +81-45-924-5359. Fax: +81-45-924-5359.
[†] Frontier Collaborative Research Center, Tokyo Institute of Technology.
[‡] Materials and Structures Laboratory, Tokyo Institute of Technology.
[§] Department of Physical Science, Graduate School of Science, Osaka Prefecture University.
[||] Structural Materials Science Laboratory, Harima Institute.
[⊥] CREST, Japan Science and Technology Agency.

10.1021/nl062717b CCC: $37.00
Published on Web 03/22/2007

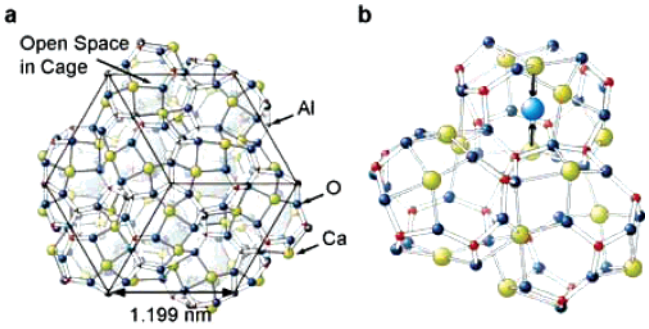

Figure 1. Crystal structure of C12A7, $[Ca_{24}Al_{28}O_{64}]^{4+}(2O^{2-})$. (a) Structure of the cage framework. Free oxygen ions are neglected for simplicity. The black box shows a cubic unit cell with twelve cages. Two of the 12 cages encage a free oxygen ion in each cage in the stoichiometric state. When each free oxygen ion is replaced by two electrons, electron occupancy in the cage is 4/12. The cage has a large free space with ~0.4 nm inner diameter. If a cage does not contain an ion, the cage forms a free-electron-like s orbital, as illustrated by the large spheres. (b) Expanded image showing three cages extracted from (a). A cage has a free oxygen ion (illustrated as a light blue sphere). Six Ca ions (green spheres) form a part of the cage wall and two Ca ions coordinate to a free oxygen ion or to an empty cage center. Upon incorporating a free oxygen ion, lattice relaxation is induced as indicated by the arrows: i.e., the ion-encaging cage shrinks, while the empty cages slightly expand.

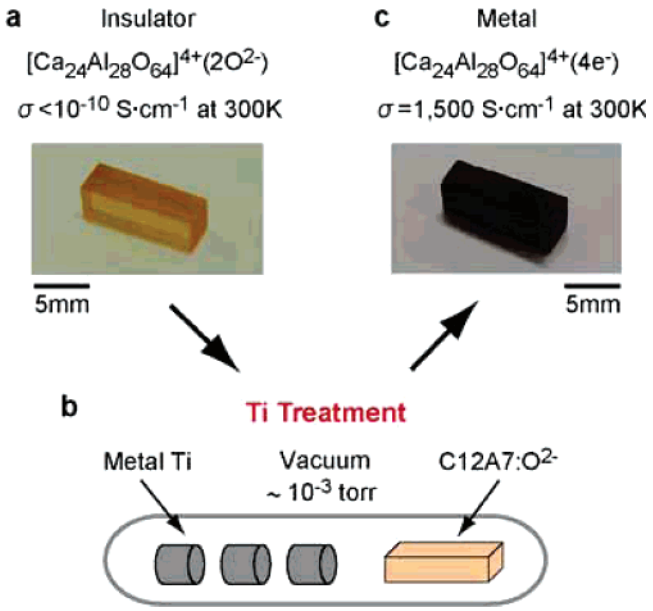

Figure 2. Conversion of insulating C12A7 to metallic C12A7. (a) Nominally undoped C12A7 is transparent with an orange tint due to the trace of Ir impurity incorporated from the Ir crucible during the CZ process. The sample is an insulator with a conductivity less than our detection limit (~10^{-10} Scm^{-1}). (b) Free oxygen ions in C12A7 are extracted by annealing with metal Ti powders at 900−1100 °C (Ti-treatment). (c) Ti-treatment turns the sample dark green and simultaneously increases electrical conductivity up to 1500 Scm^{-1} at 300 K.

show that the complete replacement of the free oxygen ions by electrons in C12A7 results in a metallic conduction with a sharp enhancement of the mobility from ~0.1 to 4 cm^2 V^{-1} s^{-1}.

We have developed several processes that enable the free oxygen ions to be replaced with electrons.[1,3,12−14] Among them, thermal annealing of C12A7 single crystals in Ca metal vapor at 700 °C led to the highest electrical conductivity of ~80 Scm^{-1} at 300 K[1] at that moment. However, the Ca treatment needs a long duration (10 days for a 0.4 mm thick sample) to extract the free oxygen ions because the annealing temperature is limited to 700 °C. Further, the replacement may be incomplete due to the formation of a surface CaO layer that acts as a diffusion barrier.[15] In this work, these drawbacks have been overcome by employing a Ti treatment because Ti forms stable nonstoichiometric oxides over a wide chemical composition range ($1 < x < 2$ in TiO_{2-x}) and the out-diffusion of the free oxygen ions from C12A7 is not blocked even if a thick titanium oxide layer completely covers the sample surface. In addition, higher annealing temperatures up to ~1300 °C can be used because Ti does not react with C12A7 up to this temperature. Because an increase in the temperature from 700 to 1100 °C enhances the diffusion of the free oxygen ions in C12A7 by several orders of magnitude,[15,16] the treatment time can be drastically shortened.

Czochralski (CZ)-grown C12A7 single crystals[17] were subjected to the Ti treatment to dope electrons (Figure 2b). The crystal was transparent, but had an orange tint (Figure 2a) due to trace Ir ions (concentration ~5×10^{17} cm^{-3}) unintentionally incorporated from the Ir crucible used in the CZ process. The Ti treatment changed the sample color from the transparent orange tint to dark green (Figure 2c), which simultaneously enhanced the electrical conductivity.

Figure 3a shows the Arrhenius plot of the electrical conductivities (σ) for the Ti-treated single crystals with different electron concentrations (N_e). The N_e values were evaluated from the optical reflection spectra of the single crystals (see Supporting Information). The Arrhenius plot has a negative slope when the electron concentration is low, indicating that a thermally activated mechanism such as hopping controls the migration of the electrons. On the other hand, the temperature dependence vanishes at $N_e \sim 9.7 \times 10^{20}$ cm^{-3} (N_{th}), demonstrating that the electron conduction is degenerated, and finally, the slope becomes positive around room temperature at larger N_e values. The conductivity extrapolated to 0 K (σ_{0K}) as a function of N_e (Figure 3b) shows this systematic change more clearly: σ_{0K} starts to increase from zero to a finite value at $N_e = N_{th}$, confirming an IM transition, and σ_{0K} superlinearly increases with N_e, showing a sharp increase in the drift mobility (from ~0.1 to 4 cm^2 V^{-1} s^{-1}) for $N_e > N_{th}$ (inset of Figure 3b).

The resistivity (ρ)−T curve of sample (d) (Figure 3c) reveals the electron−electron interaction governs ρ ($n \sim 2$ in $\rho - \rho_0 \propto AT^n$) in the temperature range below ~100 K and the phonon scattering controls ρ ($n \sim 1$ in $\rho - \rho_0 \propto AT^n$) at higher temperatures. The temperature-independent residual resistivity (ρ_0) is evidently observed at temperatures lower than ~10 K, which is likely due to imperfections of the crystal, including the impurity Ir ions and residual free oxygen ions.

Furthermore, the addition of a magnetic ion invokes a Kondo-like anomaly in the ρ−T curve. Here, we intentionally doped Ir ions to large-grained (typical grain sizes ~3 mm)

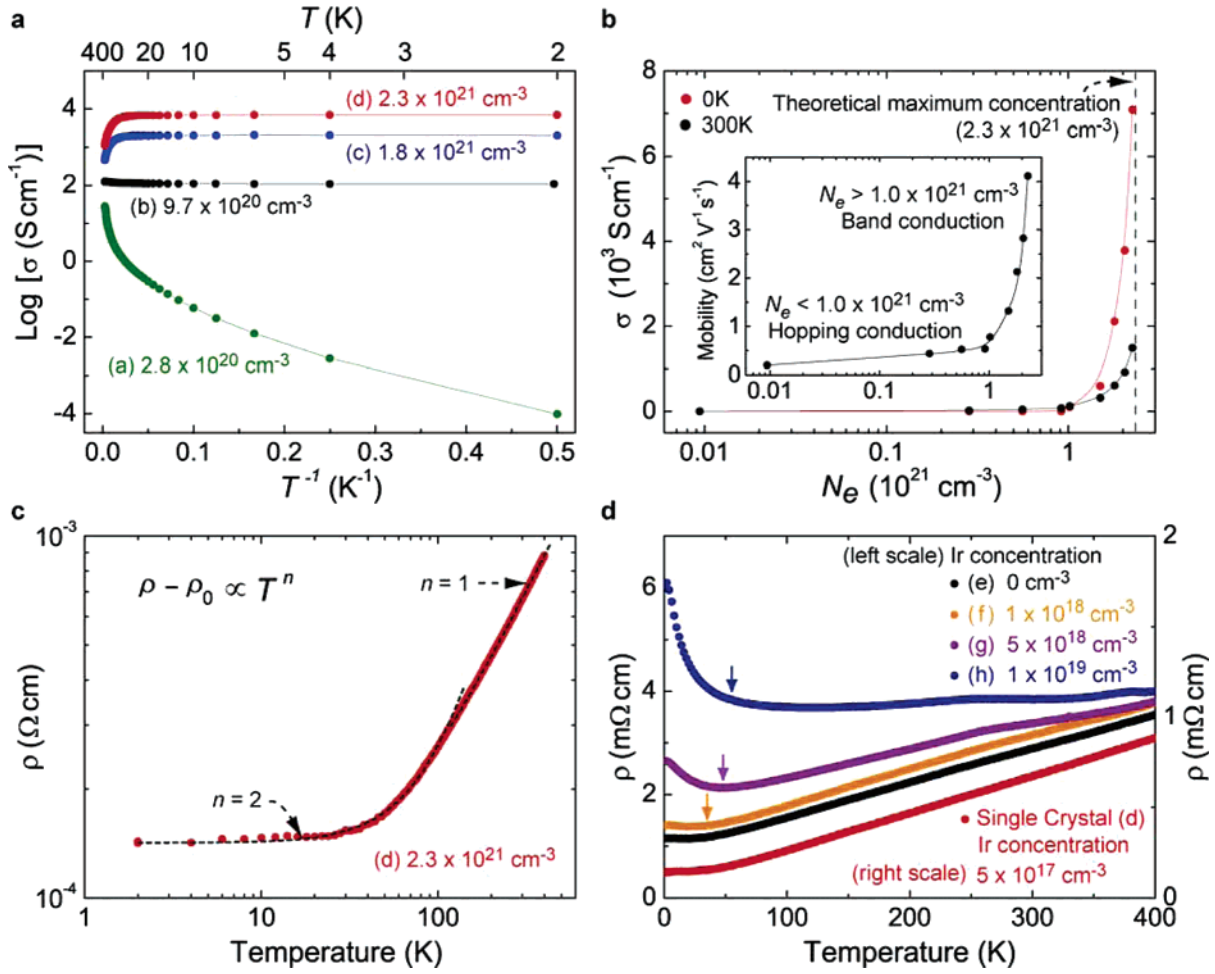

Figure 3. Electrical properties of electron-doped C12A7 single crystals and intentionally Ir-doped polycrystals. (a) Temperature dependence of conductivity (σ) for C12A7 single crystals Ti treated for (a) 700 °C, 24 h, (b) 900 °C, 24 h, (c) 1000 °C, 72 h, and (d) 1100 °C, 24 h. The values in the figure denote electron concentrations. σ increases as the treatment temperature and duration increase. The most resistive sample (a) shows a thermally activated behavior, while the conduction type changes to degeneration at $N_e = N_{th} \sim 1 \times 10^{21}$ cm^{-3}, and finally to metallic at higher N_e. (b) Insulator−metal transition. Electrical conductivities extrapolated to 0 K (σ_{0K}) are zero at $N_e < N_{th}$, but sharply increase as the carrier concentration increases at larger N_e. Electron mobilities at 300 K are low $\ll 1$ cm^2 V^{-1} s^{-1} at $N_e < N_{th}$, but sharply increase at higher N_e. (c) Electrical resistivity (ρ) of the sample (d) increases as the temperature increases and follows the $\rho - \rho_0 \propto T^n$ law with $n \sim 2$ at low temperatures, which is typical of metals. (d) Temperature dependence of electrical resistivity for Ir-doped polycrystalline $[Ca_{24}Al_{28}O_{64}]^{4+}(4e^-)$. The nominal Ir concentrations are denoted in the figure. The resistivity of the single-crystal sample (d) in Figure 3a (the analyzed Ir concentration is 5×10^{17} cm^{-3}) is shown for comparison. Temperature dependence of electrical resistivity for the Ir-free polycrystalline $[Ca_{24}Al_{28}O_{64}]^{4+}(4e^-)$ (e) is similar to that of the sample (d), although the resistivity is larger due to the grain boundary scattering. The $\rho-T$ curves have a minimum for Ir concentrations $\geq 1 \times 10^{18}$ cm^{-3}. The minimum temperatures estimated from the $[Ir]^{1/5}$ law ([Ir] is the Ir concentration) are indicated by vertical arrows, which show a reasonable agreement with the observed $\rho-T$ curves.

polycrystalline $[Ca_{24}Al_{28}O_{64}]^{4+}(4e^-)$ (see Supporting Information) up to a level of 1×10^{19} cm^{-3} (Figure 3d). ρ in the nominally pure polycrystalline samples are larger than that of the single crystal at all of the temperatures, which suggests that the grain-boundary scattering increases the resistivity to this extent. With increasing the Ir content, ρ becomes even larger, especially at low temperatures, and consequently, the $\rho-T$ curves exhibit the minimum at T_m, as indicated by arrows. The results reasonably follow the relation of the Kondo effect,[18] $T_m \propto [Ir]^{1/5}$, indicating that the interaction of the conduction electron with the electron spin moment of the Ir ion is more dominant than the other carrier-scattering mechanisms. The observation of the Kondo effect suggests that the $[Ca_{24}Al_{28}O_{64}]^{4+}(4e^-)$ is like a typical metal.

These observations demonstrate that the insulating C12A7 is converted to a metal by replacing more than half of the free oxygen ions by electrons. This IM transition accompanies a sharp increase in the drift mobility (μ_e) from $\sim$0.1 to 4 cm^2 V^{-1} s^{-1} as N_e increases. It should be noted that the doping and conduction mechanisms in C12A7 are much different from those in conventional semiconductors[19] due to the unique crystal and electronic structures of C12A7.

In typical semiconductors such as phosphorus-doped Si,[20] the IM transition occurs due to the percolative overlap of the donor wave functions, as explained by Mott in terms of the critical donor concentration N_c,[21] which follows the empirical relation $N_c^{1/3} \cdot R_c \sim 0.25$ (R_c denotes the radius of the electron orbital).[22] When the N_{th} value of $\sim 1 \times 10^{21}$ cm^{-3}

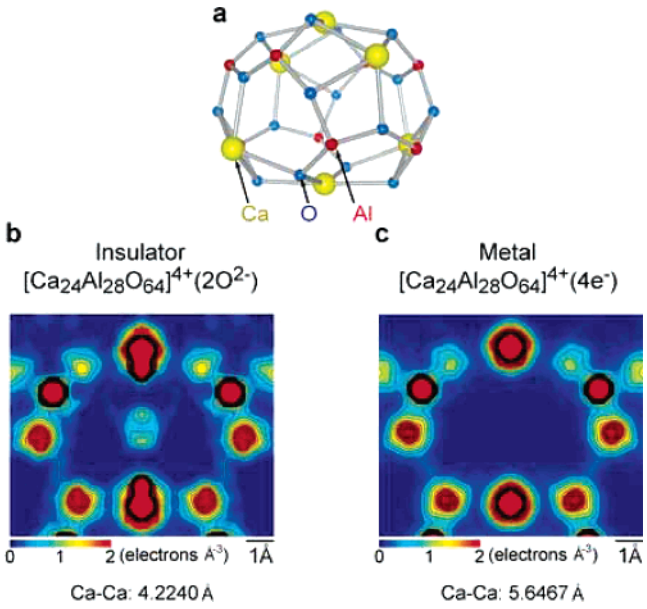

Figure 4. MEM electron density maps of C12A7. (a) An empty cage structure extracted from Figure 1a. The positions of the ions corresponds to those in parts (b) and (c). (b) MEM electron density map at the (001) plane of insulating $[Ca_{24}Al_{28}O_{64}]^{4+}(2O^{2-})$ at 90 K. The electron densities of deformed (O^{2-}-encaging) and undeformed (empty) cages are superimposed in the map, giving the dumbbell shaped densities of the Ca ions. The Ca−Ca distance in the O^{2-}-encaging cage is shown at the bottom, which is a measure of the cage deformation. (c) MEM electron density map of metallic $[Ca_{24}Al_{28}O_{64}]^{4+}(4e^-)$ at 90 K. The Ca−Ca distance in the cage is shown at the bottom.

is put into this relation, the obtained R_c value is ∼0.26 nm, which is close to the radius of the crystallographic cage embedded in C12A7 (∼0.25 nm). Thus, it is feasible that the IM transition in C12A7 occurs via the percolation of the "donor" orbitals. However, this view is not directly applicable to C12A7 because even an "undoped" stoichiometric C12A7 crystal has a "donor wavefunction" in each empty cage as a component of the CCB. Although the "donor wavefunction" intrinsically exists, the electrons doped to the CCB do not contribute to the band conduction at $N_e < N_{th}$ at low temperatures because the electron is localized in a cage forming an F^+-like center[3] due to the lattice relaxation as described above. However, a high electron doping may average out the deformations of the cage geometry throughout the crystal and it converts the localized F^+-like state to a delocalized state, invoking an IM transition.

This model for the IM transition is validated by MEM/Rietveld analysis[23,24] and ab initio density functional theory (DFT) calculations[25] (see Supporting Information). Parts b and c of Figure 4 display the electron density maps in the (001) plane of (b) stoichiometric C12A7 and (c) metallic C12A7 obtained by the MEM/Rietveld analysis. The electron densities of the Ca^{2+} ions on the cage wall of stoichiometric C12A7 have long tails like a dumbbell shape, indicating that the map is a superposition of the two deformed O^{2-}-encaging cages and the 10 undeformed empty cages. The distances between the Ca^{2+} ions (D_{Ca-Ca}) in the deformed and empty cages obtained by the Rietveld analysis are 4.22 and 5.65 Å, respectively. Thus, the map in Figure 4b provides a solid evidence that the O^{2-}-encaging cage shrinks largely from the empty cage. On the other hand, the map in Figure 4c indicates the cage structure of $[Ca_{24}Al_{28}O_{64}]^{4+}(4e^-)$ clearly differs from that of stoichiometric C12A7. Each atom has a spherical electron density, indicating that the local structural deformation is removed in $[Ca_{24}Al_{28}O_{64}]^{4+}(4e^-)$. That is, all 12 cages are homogenized and D_{Ca-Ca} (5.64 Å) becomes close to that of the empty cage, suggesting the electrons are distributed uniformly over the 12 cages within an accuracy of the MEM/Rietveld analysis.

Figure 5 shows relaxed lattice structures calculated by DFT with the isosurfaces of the wave function ($|\Psi|^2$) of the 2p level of the free oxygen ions (Figure 5a) and those of CCB bottom (isosurface state density) (Figure 5b) for (i) stoichiometric C12A7, (ii) $[Ca_{24}Al_{28}O_{64}]^{4+}(O^{2-})\cdot(2e^-)$, and (iii) metallic C12A7. The DFT results are summarized in Figure 5c as a schematic energy level diagram. Figure 5a(i) demonstrates that two free oxygen ions respectively occupy the cages at the center and the corners of the unit cell and the other cages are empty in the stoichiometric C12A7. The calculated D_{Ca-Ca} of the O^{2-}-encaging cage is 4.27 Å, in good agreement with the observed value of 4.22 Å. Further, each empty cage has an s-like state, and the connection of these states forms the CCB even in the stoichiometric C12A7 (Figure 5b(i)). On the other hand, the O^{2-}-encaging cage has no such CCB state because of the entrapping of O^{2-}, whose 2p energy level is located slightly above the valence band maximum of the cage framework (Figure 5c(i)) Thus, stoichiometric C12A7 has no electron in the CCB and is a band insulator.

The DFT result for $[Ca_{24}Al_{28}O_{64}]^{4+}(O^{2-})\cdot(2e^-)$, where a free oxygen ion is extracted from a cage and two electrons occupy two of the other cages in the unit cell, demonstrates that D_{Ca-Ca} (5.57 Å) of the electron-encaging cage becomes larger compared to that of the O^{2-}-encaging cage (4.27 Å), but it is still smaller than that of the empty cage (5.77 Å). The wave function at the CCB minimum (Figure 5b(ii)) implies that the electron is still localized in a specific cage, forming an F^+-like center (Figure 5c(ii)).

Figure 5b(iii) is the relaxed lattice structure with the isosurface state density at the CCB minimum of $[Ca_{24}Al_{28}O_{64}]^{4+}(4e^-)$, revealing that D_{Ca-Ca} (5.63 Å) of the electron-encaging cage further expands from that of $[Ca_{24}Al_{28}O_{64}]^{4+}(O^{2-})\cdot(2e^-)$ and it becomes very close to that of the empty cage. It also indicates the isosurface state density in each cage is equivalent, indicating that the electrons are delocalized over the cages and consequently the cage conduction band has a rather large dispersion of ∼2 eV (Figure 5c(iii)).

Thus, the DFT calculation, consistent with the MEM/Rietveld analysis, qualitatively explains why the C12A7 shows the IM transition upon the electron doping. That is, the successive reduction of deformation of the electron-encaging cage with increasing the electron concentration induces the IM transition, which accompanies the sharp increase in the electron mobility. It is noteworthy that simple ionic oxides such as MgO have not exhibited such a high conductive state, although the F/F^+-like centers can be

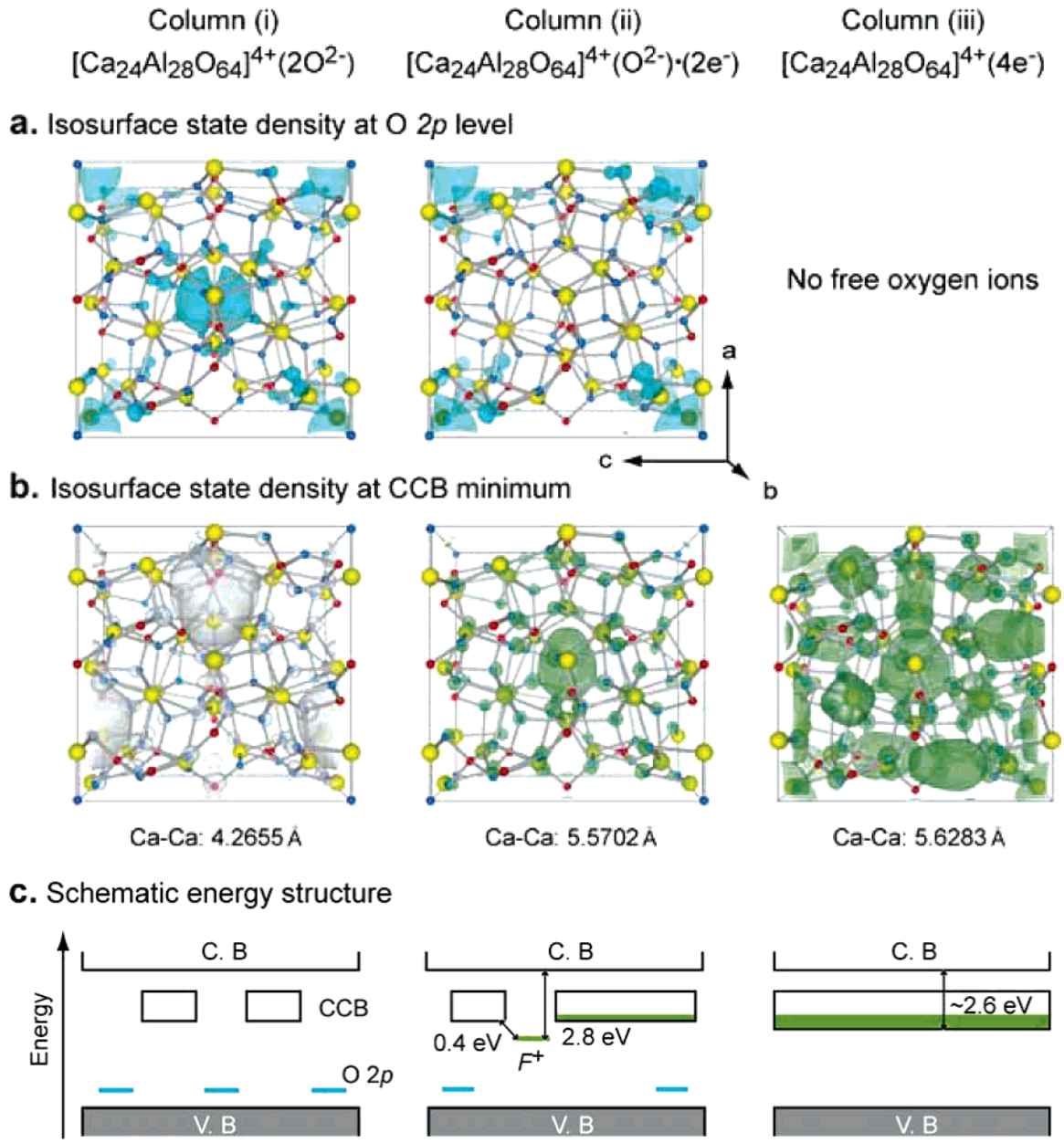

Figure 5. Relaxed lattice structures and electronic structures of C12A7 having three different electron concentrations: (i) stoichiometric $[Ca_{24}Al_{28}O_{64}]^{4+}(2O^{2-})$, (ii) $[Ca_{24}Al_{28}O_{64}]^{4+}(O^{2-})\cdot(2e^{-})$, and (iii) $[Ca_{24}Al_{28}O_{64}]^{4+}(4e^{-})$. (a,b) DFT isosurface state density of (a) the HOMO levels of the free oxygen ions and (b) the CCB bottom levels. Each box represents the unit cell. The blue and green color denotes the electron density maps for 2p electron of the free oxygen ions and the CCB electrons, respectively. The gray color denotes the s-like density of states in empty cages. The values of the isosurfaces are $5 \times 10^{-3}e^{-}/Å^3$ for (a(i)), (a(ii)), (b(i)), and (b(ii)), and $2.5 \times 10^{-3}e^{-}/Å^3$ for (b(iii)). (c) Schematic energy structures. Blue and green show the occupied levels of free oxygen ions and electrons in the cages, respectively.

incorporated at high concentrations similar to the present case.[26,27] Thus, the three-dimensionally connected sub-nanometer-sized cage structure in C12A7 plays an essential role in the appearance of the metallic state.

In summary, an IM transition is observed for the first time in a light metal oxide. The keys to realizing metallic C12A7 are to utilize the free space of the cages embedded in the unique nanostructure of the C12A7 crystal and to suppress the local lattice relaxation upon the electron doping. The present finding of a metal composed of well-known insulators, CaO and Al_2O_3, demonstrates the potential of a closely packed three-dimensional nanostructure embedded in a crystal, which may lead to cultivation of electroactive functions using only abundant materials such as light metal oxides that have not been regarded as a source of functional materials.

Acknowledgment. This work was supported by a Grant-in-Aid for Creative Scientific Research (no. 16GS0205) from Japanese Ministry of Education, Culture, Sports, Science, and Technology. X-ray diffraction study was supported by CREST/JST and JASRI/SPring-8 Nanotechnology Support Project of the Ministry of Education, Culture, Sports, Science, and Technology of Japan. We thank Drs. K. Kato, K. Osaka,

M. Miyakawa, K. Kawamura, and J. E. Kim for the kind advice and support in data collection and Dr. H. Tanaka for the computer program ENIGMA for the MEM analysis.

Supporting Information Available: Materials synthesis, measurement of electron concentration, electrical measurements, XRD and MEM/Rietveld analysis, electronic structure calculation. This material is available free of charge via the Internet at http://pubs.acs.org.

Note Added after ASAP Publication. This paper was published ASAP on March 22, 2007. Reference 7 was updated to include a second source. The revised paper was reposted on April 2, 2007.

References

(1) Matsuishi, S.; Toda, Y.; Miyakawa, M.; Hayashi, K.; Kamiya, T.; Hirano, M.; Tanaka, I.; Hosono, H. *Science* **2003**, *301*, 626−629.
(2) Dye, J. L. *Inorg. Chem.* **1997**, *36*, 3816−3826.
(3) Hayashi, K.; Matsuishi, S.; Kamiya, T.; Hirano, M.; Hosono, H. *Nature* **2002**, *419*, 462−465.
(4) Bartl, H.; Scheller, T. *Neues Jahrb. Mineral., Monatsh.* **1970**, *35*, 547−552.
(5) Hosono, H.; Abe, Y. *Inorg. Chem.* **1987**, *26*, 1192−1195.
(6) Hayashi, K.; Hirano, M.; Matsuishi, S.; Hosono, H. *J. Am. Chem. Soc.* **2002**, *124*, 738−739.
(7) Sushko, P. V.; Schluger, A. L.; Hayashi, K.; Hirano, M.; Hosono, H. *Phys. Rev. Lett.* **2003**, *91*, 126401. Sushko, P. V.; Schluger, A. L.; Hayashi, K.; Hirano, M.; Hosono, H. *Thin Solid Films* **2003**, *445*, 161−167.
(8) Toda, Y.; Matuishi, S.; Hayashi, K.; Ueda, K.; Kamiya, T.; Hirano, M.; Hosono, H. *Adv. Mater.* **2004**, *16*, 685−689.
(9) Li, Z.; Yang, J.; Hou, J. G.; Zhu, Q. *Angew. Chem., Int. Ed.* **2004**, *43*, 6479−6482.
(10) Bertoni, M. I.; Mason, T. O.; Medvedeva, J. E.; Freeman, A. J.; Poeppelmeier, K. R.; Delley, B. *J. Appl. Phys.* **2005**, *97*, 103713.
(11) Medvedeva, J. E.; Freeman, A. J. *Appl. Phys. Lett.* **2004**, *85*, 955−957.
(12) Kim, S. W.; Miyakawa, M.; Hayashi, K.; Sakai, T.; Hirano, M.; Hosono, H. *J. Am. Chem. Soc.* **2005**, *127*, 1370−1371.
(13) Miyakawa, M.; Toda, Y.; Hayashi, K.; Hirano, M.; Kamiya, T.; Matsunami, N.; Hosono, H. *J. Appl. Phys.* **2005**, *97*, 023510.
(14) The treatment temperature of the Ca treatment is limited to below ∼700 °C, otherwise C12A7 reacts with Ca. In addition, the extraction of the free oxygen ions by Ca vapor consequently forms a CaO layer, which works as a barrier for out-diffusion of the free oxygen ion. These two factors make complete replacement of the free oxygen ions by electrons almost impossible.
(15) Lacerda, M.; Irvine, J. T. S.; Glasser, F. P.; West, A. R. *Nature* **1988**, *332*, 525−526.
(16) Lacerda, M.; West, A. R.; Irvine, J. T. S. *Solid State Ionics* **1993**, *59*, 257−262.
(17) Kurashige, K.; Toda, Y.; Matuishi, S.; Hayashi, K.; Ueda, K.; Kamiya, T.; Hirano, M.; Hosono. *Cryst. Growth Des.* **2006**, *6*, 1602−1605.
(18) Kondo, J. *Solid State Phys.* **1969**, *23*, 183.
(19) Imada, M.; Fujimori, A.; Tokura, Y. *Rev. Mod. Phys.* **1998**, *70*, 1039−1263.
(20) v. Löhneysen, H. *Curr. Opin. Solid State Mater. Sci.* **1998**, *3*, 5−15.
(21) Mott, N. F. *Metal−Insulator Transitions*; Taylor & Francis: London, 1990.
(22) Edwards, P. P.; Sienko, M. J. *J. Am. Chem. Soc.* **1981**, *103*, 2967−2971.
(23) Takata, M.; Nishibori, E.; Sakata, M. *Z. Kristallogr.* **2001**, *216*, 71−86.
(24) Kitaura, R.; Kitagawa, S.; Kubota, Y.; Kobayashi, T. C.; Kindo, K.; Mita, Y.; Matsuo, A.; Kobayashi, A.; Chang, H. C.; Ozawa, T. C.; Suzuki, M.; Sakata, M.; Takata, M. *Science* **2002**, *298*, 2358−2361.
(25) Kresse, G.; Furthmüller. J. *Phys. Rev. B* **1996**, *54*, 11169−11186.
(26) Ion implantation of Li^+ to an MgO single crystal created F^+ centers up to 1.6×10^{21} cm^{-3}, but the maximum conductivity attained remains only 6×10^{-5} Scm^{-1} at RT.[27] This sharp contrast to the electron-doped C12A7 makes it clear that the 3D-connected subnanometer-sized cages are essentially important for the emergence of metallic state.
(27) Tardío, M.; Ramírez, R.; González, R.; Chen, Y.; Alves, E. *Phys. Res. B* **2002**, *191*, 191−195.

NL062717B